

Article

Stability Condition of Methane Hydrate in Fine-Grained Sediment

Di Lu ¹, Qin Tang ², Dehuan Yang ³, Rongtao Yan ^{1,*}, Yun Chen ¹ and Shuai Tao ^{4,*}

¹ Guangxi Key Laboratory of Geomechanics and Geotechnical Engineering, Guilin University of Technology, Guilin 541004, China

² School of Environmental Science and Engineering, Sun Yat-Sen University, Guangzhou 510275, China

³ School of Architecture and Transportation Engineering, Guilin University of Electronic Technology, Guilin 541004, China

⁴ POWERCHINA Huadong Engineering Corporation Limited, Hangzhou 310014, China

* Correspondence: 2012019@glut.edu.cn (R.Y.); tao_s@hdec.com (S.T.)

Abstract: Stability condition is of critical importance for methane hydrate exploitation, transportation, and reserves. This study measured the stability conditions of methane hydrate in fine-grained sediment with different dry densities ($\rho_d = 1.40, 1.50$ and 1.60 g/cm^3) and various initial water saturations by the multi-step heating method. The experimental result showed that the methane hydrate formation in fine-grained sediment required lower temperature and/or higher pressure compared to that in bulk state. At the same time, it is found that the deviation degree of P–T conditions of methane hydrate in fine-grained sediment with different dry density and initial water saturation are completely different from that in pure water. In addition, according to the nuclear magnetic resonance technique (NMR), the changes in NMR signal intensity during the formation and decomposition of methane hydrate in silt were analyzed. Regardless of formation and dissociation stages, liquid water always distributes in the small sediment pores. An empirical formula is developed to address the capillary suction of water and hydrate with respect to the unhydrated water within sediment. Furthermore, a phase equilibrium model is proposed to predict the stability conditions of hydrate-bearing fine-grained sediment.

Keywords: fine-grained sediment; methane hydrate; stability conditions; nuclear magnetic resonance; phase equilibrium model



Citation: Lu, D.; Tang, Q.; Yang, D.; Yan, R.; Chen, Y.; Tao, S. Stability Condition of Methane Hydrate in Fine-Grained Sediment. *J. Mar. Sci. Eng.* **2023**, *11*, 196. <https://doi.org/10.3390/jmse11010196>

Academic Editor: Timothy S. Collett

Received: 13 November 2022

Revised: 24 December 2022

Accepted: 30 December 2022

Published: 12 January 2023



Copyright: © 2023 by the authors. Licensee MDPI, Basel, Switzerland. This article is an open access article distributed under the terms and conditions of the Creative Commons Attribution (CC BY) license (<https://creativecommons.org/licenses/by/4.0/>).

1. Introduction

Natural gas hydrate (NGH) is a cage-type crystalline ice-like solid formed by natural gas and water molecules under high pressure and low temperature, which mainly occurs in the permafrost region and deep-sea sediment environment [1,2]. Due to the high methane density of NGH, and the huge reserves throughout the world, methane hydrate is considered as a potential clean energy in the 21st century [3,4]. The traditional hydrate exploitation methods include depressurization, thermal injection, and chemical injection, which drives methane hydrate from stable state to unstable state for dissociating methane hydrate back into gas and water [5]. Then, the methane gas is extracted and collected as an energy resource. Therefore, understanding the stability condition of methane hydrate within sediment and establishing the corresponding thermodynamic model are of importance for designing the exploitation scheme for methane hydrate. Moreover, the developed model is helpful to evaluate the productive efficiency for methane hydrate.

To meet the requirement of commercial exploitation of hydrate, many scholars have performed research on the stability conditions of hydrate in bulk state or within sediment. Early researchers [6,7] focused on the stability condition of bulk hydrate and obtained a great deal of experimental data. However, this research result is not applicable to the actual exploitation of gas hydrate. Because in the process of hydrate formation, the water

in natural sediments will be subject to the physical and chemical action from soil particles, thus changing the stability conditions of methane hydrate. Thus, the stability condition of bulk hydrate is not applicable to analyze the hydrate synthesizing or dissociation behavior within sediment [8]. Subsequently, researchers began to synthesize hydrate in porous media and measured the stability condition of hydrate.

Handa and Stupin [9] measured the stability conditions of propane hydrate and methane hydrate within silica geo material with particle size of 200~425 mesh. The experimental result showed that the stable pressure for the silica geo material was 20~100% higher than that for bulk state. A similar observation was obtained by Uchida et al. [10–12] through measuring the stability condition of hydrate in glass beads. Linga et al. [13] studied the formation of methane hydrate in quartz sand and concluded that the conversion rate of methane hydrate in quartz sand is about 75%. Bagherzadeh et al. [14] used NMR to study the synthesis of methane hydrate in quartz sand with different particle sizes and found that the smaller particle size of porous media corresponded to the faster hydrate formation rate and the lower the residual water content. Clennell et al. [8] insisted that the influence of hydrate occurrence on hydrate stability was attributed to the fact that the physicochemical interactions between water and sediment reduced the chemical potential of pore water. Turner et al. [15] found that the pore size has little effect on the stability condition of hydrate when the pore size is greater than 60 nm. However, most studies adopted that synthetic material as the host sediment, and thus the pore distribution range was narrow, which could not reflect the pore characteristics and mineral composition of natural hydrate sediments.

In the South China Sea, natural gas hydrate is mainly distributed in the sediments containing clay [16–18]. The existing research has shown that the pore size and distribution of sediments have a significant impact on dissociation behavior of hydrate [19]. Kumar et al. [20] found that the conversion rate and formation rate of hydrate in quartz sand sediments decreased after the addition of clay. Compared to the synthetic materials with single pore size, the pore characteristics of clay sediments are more complex, and the capillary effect of small pores will lead to lower water activity [8,9]. The charge on the surface of clay minerals also leads to more complex physicochemical interactions of water molecules on the clay surface. Furthermore, seismic wave attenuation known by its high sensitivity to porosity, permeability and fluid content (e.g., Matsushima et al. [21]), was used by Bouchaala et al. [22] to detect and study the stability of hydrates in the North Sea. Meanwhile, they found a good correlation between field and laboratory results.

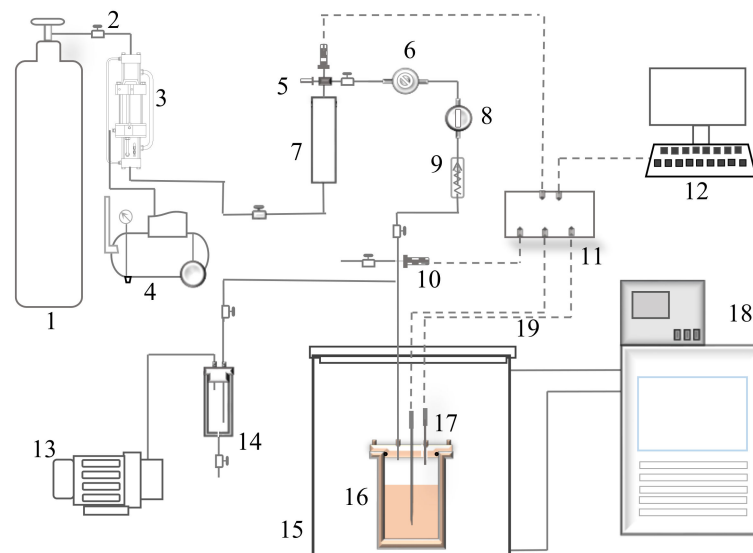
To further explore the stable condition of hydrate in sediments, Uchida et al. [20,23,24] analyzed the effect of small pore size in clay mineral sediments on hydrate stability from the aspect of thermodynamics. However, the experimental data of hydrate stability conditions in seafloor clay sediments insufficiently meet the current needs, especially in revealing the micro influence mechanism on hydrate stability conditions in the South China Sea. To this end, this paper refers to sediment characteristic (GMGS3 [25]) in the South China Sea to prepare the synthetic samples. The stable condition of methane hydrate was measured for analyzing the sediment capillary influence. In addition, Nuclear Magnetic Resonance was also used to further explore the phase transition mechanism of methane hydrate in sediments with different pore sizes. At present, there are not many data for testing hydrate by NMR technology, and this work can quantify the change in unhydrated water in the process of hydrate formation without damaging the sample, which is of great significance for studying the stable conditions of hydrate synthesis in sediment. Moreover, a modified model was employed to characterize the stable condition of methane hydrate within sediment.

2. Experimental Introductions

2.1. Experimental Equipment and Procedures

2.1.1. Stability Conditions Measurement

The schematic diagram of apparatus for measuring the stability condition is shown in Figure 1. The experimental apparatus can provide a low-temperature and high-pressure condition for hydrate formation and dissociation to measure the stability condition of methane. The flange type chamber is made of 316 stainless steel, with 148.7 mm height and 99.8 inner diameter. The maximum bearable pressure is 20 MPa. In the experiment, a high precision constant temperature water bath (controllable temperature of $-20\text{ }^{\circ}\text{C}$ to $100\text{ }^{\circ}\text{C}$, precision of $\pm 0.1\text{ }^{\circ}\text{C}$) was used to maintain the temperature of the reactor, and the ethylene glycol solution was selected as the constant temperature circulating liquid. Two Pt100 platinum resistance temperature sensors were inserted into the reactor to monitor the temperature of specimen, and the accuracy is $\pm 0.1\text{ }^{\circ}\text{C}$. A pressure sensor with measuring range of 0 to 15 MPa and accuracy of 0.1% full scale was used for measuring the pressure.



1 Gas storage tank, 2 Manual valve, 3 Gas booster pump, 4 Air compressor, 5 Safety valve, 6 Pressure regulating valve, 7 Gas storage tank, 8 Gas Flowmeter, 9 One-way valve, 10 Pressure transducer, 11 Data acquisition, 12 Computers, 13 Vacuum pump, 14 Vacuum container, 15 Water bath box, 16 Reaction kettle, 17 Temperature sensor, 18 Constant temperature flume, 19 Signal line

Figure 1. Schematic diagram of apparatus for measuring the stability conditions of methane hydrate.

In the experiment, methane hydrate was synthesized by the excess gas method. In the process of experimental operation, a vacuum pump is used to vacuum the reactor and pipeline, then methane is used for scavenging, and then vacuum and gas injection are carried out. To ensure the balance of the temperature and pressure conditions of the sample and leak detection, after the completion of gas injection, the pressure was kept stable for more than 6 h, and then the cooling synthesis was carried out. After the completion of the synthesis, the stable point data are obtained by multi-stage heating, and the step of heating is $0.5\text{ }^{\circ}\text{C}$. When the temperature and pressure condition is outside the stability line of pure hydrate, the temperature is raised to the initial value. The time for each stable point is about 6 h. This experiment mainly focuses on soil samples with different dry density ($\rho_d = 1.4, 1.5, \text{ and } 1.6\text{ g/cm}^3$) and different initial water saturation. The basic situation of the samples is shown in Table 1.

Table 1. Detailed information of tests.

NO	$\rho_d/g \cdot cm^3$	$T_{0i}^{①}/K$	$P_i^{②}/MPa$	$T_d^{③}/K$	$S_{w0}^{④}/\%$
A1	1.6	291.23	7.99	273.86	19.54
A2	1.6	291.23	8.00	273.86	48.01
B1	1.5	291.03	7.98	273.56	20.14
B2	1.5	291.43	7.98	273.76	30.13
B3	1.5	291.03	8.02	273.56	39.22
B4	1.5	291.23	7.98	273.76	50.14
C1	1.4	291.13	8.01	273.76	20.06

Annotation: ① represents the initial stable temperature of the experiment; ② represents the initial stable pressure of the experiment; ③ represents the stable temperature after hydrate formation; ④ represents the initial water saturation of the experiment.

2.1.2. NMR Experiment

The experimental equipment is made up of a MacroMR12-150H-I large aperture nuclear magnetic resonance imaging analyzer developed by Suzhou Newmai Company, which integrated with a temperature, pressure, and automatic acquisition system (Figure 2). The cavity size of the flexible button reaction tank (made of imported polyether ether ketone (PEEK)) is 70 mm length and 99.8 mm inner diameter, and withstands a pressure of 15 MPa. The temperature control layer between the outer layer of the reactor and the temperature control inner layer of the clamp is separated by two types of coolant. The coolant is the low signal strength electronic fluorination liquid (FC-770 and FC-40) produced by 3 M Company in the United States [26,27]. FC-770 coolant is used to control the sample temperature, and FC-40 coolant is used to prevent the influence of FC-770 coolant temperature on the clamp coil. The circulating coolant temperature is independently controlled by two constant temperature water baths, THGD-3030 (the controllable temperature is $-20\text{ }^\circ\text{C}$ to $100\text{ }^\circ\text{C}$, with an accuracy of $\pm 0.02\text{ }^\circ\text{C}$) and THS-30 (the controllable temperature is from room temperature to $100\text{ }^\circ\text{C}$, with an accuracy of $\pm 0.02\text{ }^\circ\text{C}$ to $0.05\text{ }^\circ\text{C}$) produced in Ningbo Tianheng instrument Factory. The temperature and pressure are measured by the optical fiber temperature sensor and the pressure sensor, and the collected data are automatically recorded on the computer. The accuracies in the temperature and pressure were $\pm 0.1\text{ }^\circ\text{C}$ and full scale, respectively.

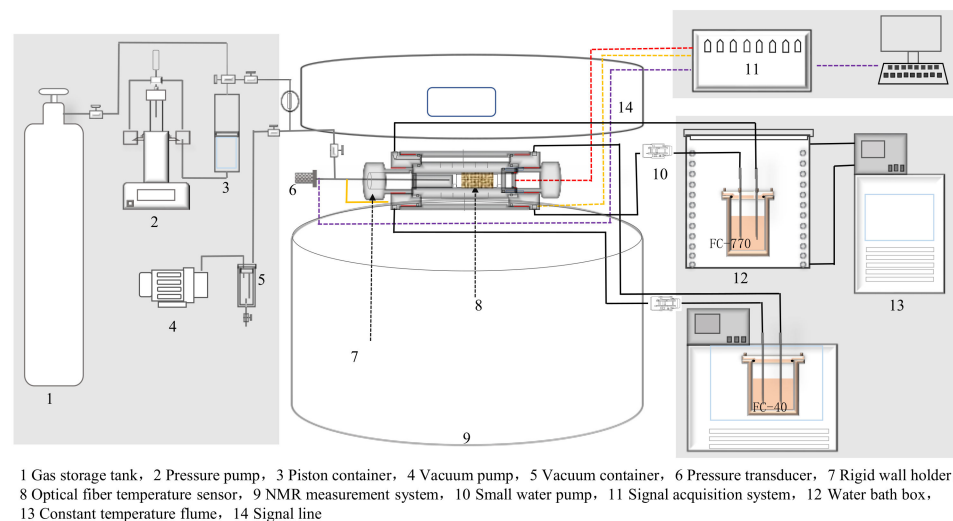


Figure 2. Nuclear magnetic resonance measurement system of natural gas hydrate.

According to a large number of previous laboratory studies [28–30], the relaxation signal of hydrogen in pore fluid measured by low-field NMR is invisible, so the formation and dissociation of hydrate in porous media can be determined by the NMR technique. The experimental operation process was as follows: the dried soil was mixed with a certain

proportion of deionized water, and then placed in a moisturizing tank for more than 24 h with a sealed bag, and the water content was measured again. The soil sample was divided into two layers and pressed into the PEEK sample tube (size 50 mm length and 29 mm inner diameter) by a Jack, then weighed and recorded. After calibrating the instrument, the signal intensity of the empty cylinder was measured first, and then the sample was put into the reactor to connect the pipeline. In order to keep the sample temperature consistent within specimen, CPMG measurement was carried out after standing for 6 h. In the following, the gas was injected into the chamber, and then decreasing the temperature forms methane hydrate. For dissociation methane hydrate, the temperature raised as 2 °C→3 °C→4 °C→5 °C→6 °C→7 °C→9 °C→10 °C→19 °C step by step. For each step, the CPMG sequence measurement was carried out after the temperature and pressure of each stage remained constant for more than 6 h. The testing conditions of the sample are shown in Table 2.

Table 2. Detailed information of tests.

NO	$\rho_d/g \cdot cm^3$	$T_{0i}^{①}/K$	$P_i^{②}/MPa$	$T_d^{③}/K$	$S_{w0}^{④}/\%$
H1	1.6	291.98	8.00	275.24	48.10
H2	1.6	292.07	8.00	274.97	20.40
H3	1.5	292.07	8.00	275.15	41.00
H4	1.4	292.07	7.99	274.97	20.30

Annotation: ① represents the initial stable temperature of the experiment; ② represents the initial stable pressure of the experiment; ③ represents the stable temperature after hydrate formation; ④ represents the initial water saturation of the experiment.

2.2. Experimental Materials

Referring to the particle content of drilling investigation borehole sampling (GMGS3 [25]) in the South China Sea God Fox Sea (Figure 3), the experimental soil is artificially prepared. Figure 3 shows the particle size distribution curve of soil sample, in which the contents of clay particle (<0.005 mm), silt particle (0.005 mm~0.075 mm), and sand particle (0.075 mm~2 mm) are 20%, 70%, and 10%, respectively. The specific gravity of the prepared soil sample is 2.73, the liquid limit is 20.06%, and the plastic limit is 14.03%. The water used in the experiment is deionized water prepared in the laboratory (conductivity 1.8 $\mu s/cm$, pH 5.6). The gas used in the test is methane gas with a purity of 99.99% purchased from Guangdong Huate Gas Co., Ltd., Foshan, China.

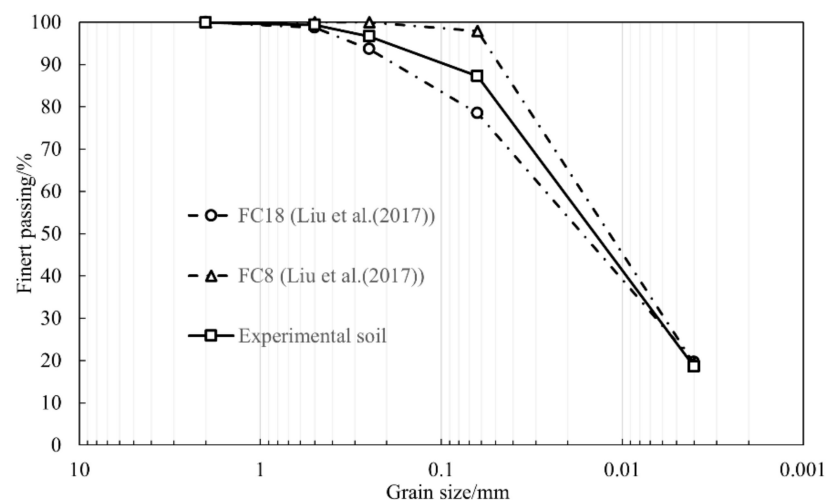


Figure 3. Comparison of the particle size distribution curve of soil sample and GMGS3 [25].

2.3. Determination of Hydrate Saturation

The hydrate saturation in the sample is defined as the ratio of the synthetic hydrate volume to the total pore volume of the sample as:

$$Sh = V_h / V_v \times 100\% \tag{1}$$

$$V_h = \Delta n_h \cdot (M_{CH_4} + M_{H_2O} \cdot N_{hyd}) / \rho_h \tag{2}$$

where Sh is Hydrate saturation, V_h is the volume of hydrate in sediment pores, N_{hyd} is the number of hydrate, here 6.1 [20,31], ρ_h is the density of hydrate (0.917 g/cm³) [32], M_{CH_4} is the molar mass of methane gas, M_{H_2O} is the molar mass of water, and Δn_h is the mass of synthetic hydrate. The experiment is carried out in a space of constant volume. According to the quantity conservation of matter, Δn_g is the methane gas consumption and can be calculated from the following gas equation of state [33]:

$$\Delta n_g = (P_i V) / (Z_i R T_i) - (P V) / (Z R T) \tag{3}$$

where P represents the pressure in the reactor, T represents the temperature of the sample, R represents the ideal gas constant (8.314 J·mol⁻¹·K⁻¹), V represents the volume of free methane gas, Z represents the gas compression factor, which is calculated according to the Peng-Robinson equation [34], and the subscript i represents the corresponding parameters in the initial state.

3. Results and Discussion

3.1. Experimental Results of Phase Equilibrium

Taking the experimental results of B1 sample as an example, Figure 4 presents the pressure and temperature of methane hydrate during formation and dissociation stages., in which the six turning points A, B, C, D, E, and F correspond to the points on the temperature and pressure curve against time (Figure 5). The stable conditions of methane hydrate in the sample can be determined from the changes of temperature and pressure against time.

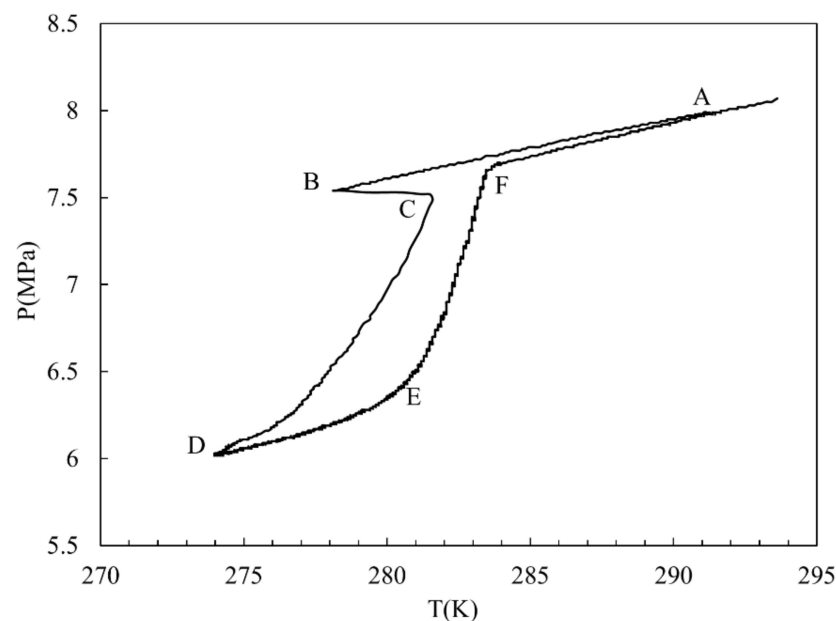


Figure 4. P–T diagram of synthesis and decomposition of methane hydrate in silt.

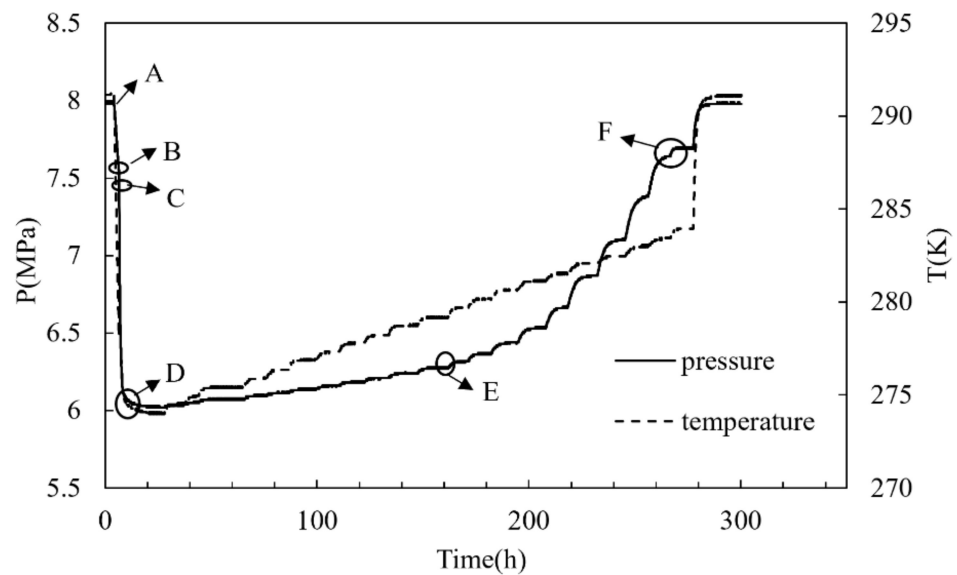
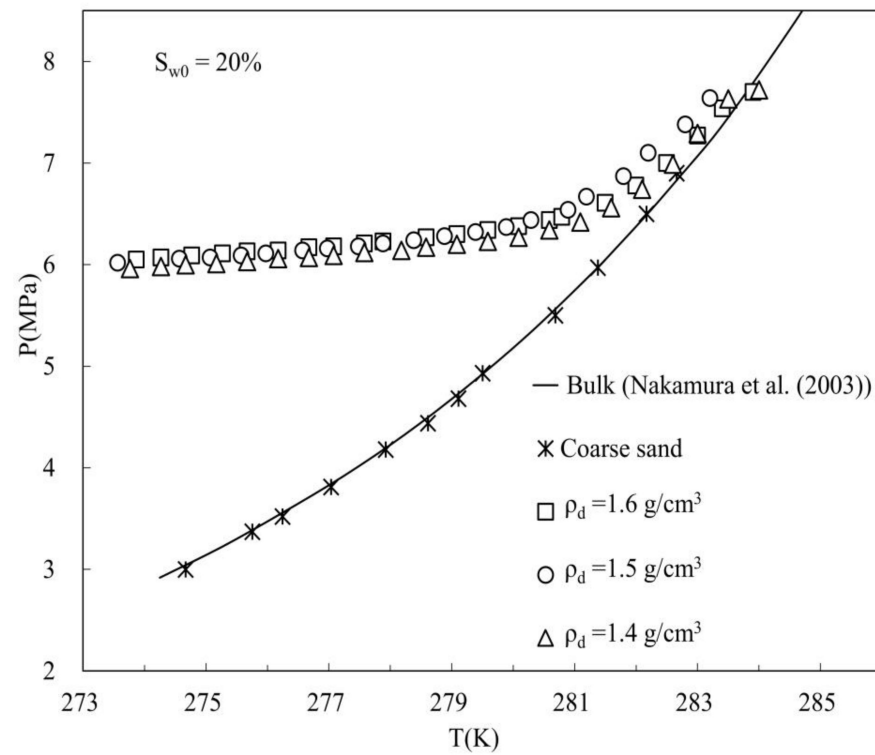


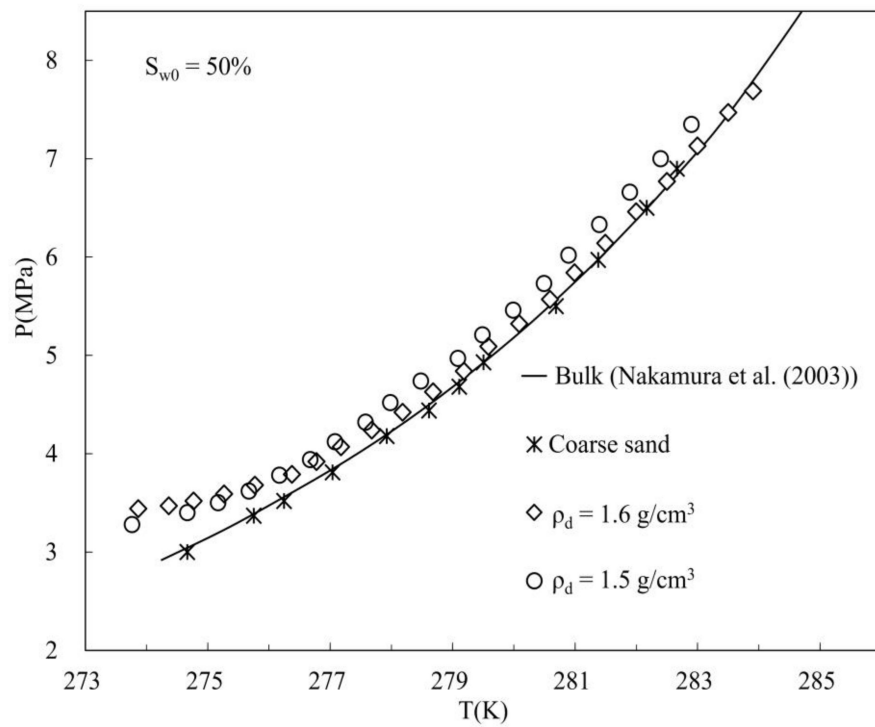
Figure 5. Pressure and temperature variation diagram of methane hydrate in fine-grained sediment.

In Figure 4, the pressure drop is flat from A to B, which indicates that the A–B section is only the volume compression of methane gas caused by the decreasing temperature. In the process from B to C, one can find an abrupt increase in temperature. This is because that a large number of hydrate nucleates and generates and releases a large amount of heat in a short time, which leads to the abnormal change in sample temperature. In the stage of C–D, the formation of hydrate gradually consumes the methane gas in the reactor, which leads to a significant decrease in pressure in the reactor with constant volume. From point D, the temperature begins to increase and dissociate methane hydrate. The generated methane gas gradually increases the gas pressure in the reactor, such as stage D–E–F. As for the F–A stage, the methane hydrate has almost been decomposed, but there is still some residual methane hydrate crystal lattice, so it is not parallel to the A–B segment. As temperature further increases, methane hydrate crystal lattice is completely decomposed, and the pressure is back to the initial point A.

Figures 6 and 7 present the stability conditions of methane hydrate of fine-grained sediment with different dry densities and initial water saturation. In addition, the stability conditions of methane hydrate in coarse sand ($0.5 \text{ mm} < \text{diameter} < 2 \text{ mm}$, $S_{W0} = 50.8\%$) were also provided for comparison. The stability conditions of methane hydrate for the coarse sand are consistent with those of pure hydrate measured by Nakamura et al. [35]. In addition, previous studies [36–38] also show that the stability conditions of hydrate in coarse sand are not affected by pores, which indicates that the experimental equipment and methods are reliable. Figure 6 shows that the stability condition curves of methane hydrate within fine-grained sediment shift left compared to those of bulk hydrate. That is to say, the methane hydrate requires higher pressure and/or lower temperature to maintain the stable state within fine-grained sediment. This is because the capillary effect decreases the activity of pore water within fine-grained sediment. In Figure 6, one also finds that the dry density has a slight influence on the stability condition curve. On the whole, high dry density corresponds to a low temperature and high pressure. However, the tendency could be affected by the hydrate saturation. Even at the same temperature, different hydrate saturation and liquid water content determine the hydrate phase transition position within fine-grained sediment. Consequently, the capillary suction can be significantly affected.



(a)



(b)

Figure 6. The stability conditions of methane hydrate in fine-grained sediment under different dry densities. (a) Low initial water saturation and bulk data [35]; (b) high initial water saturation and bulk data [35].

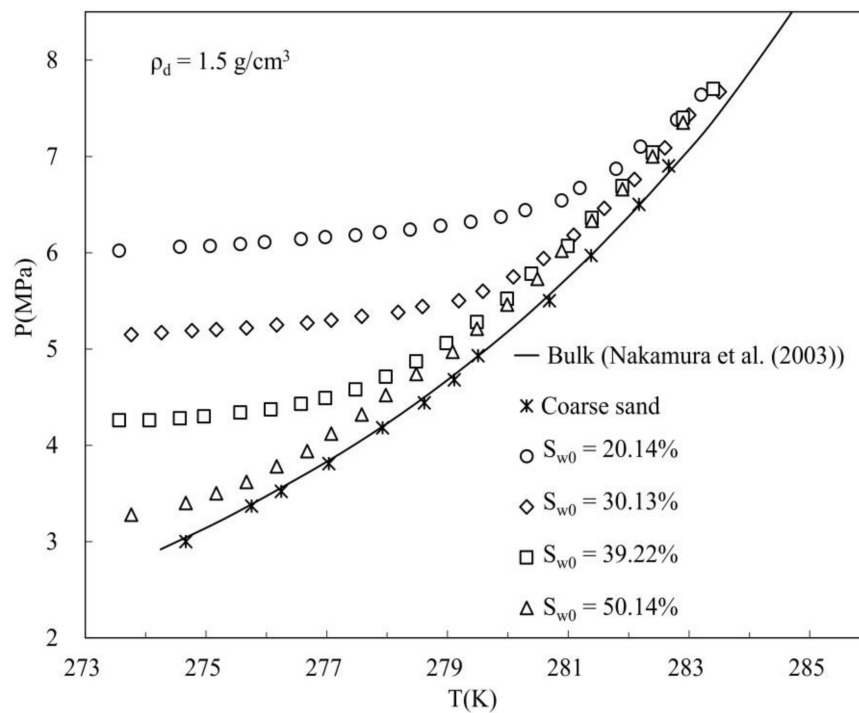
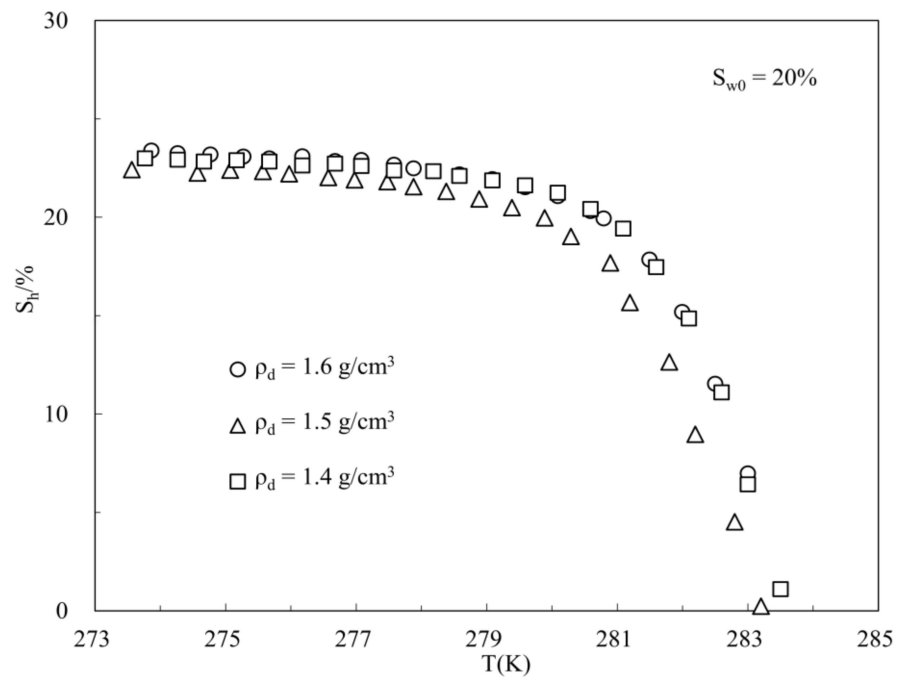


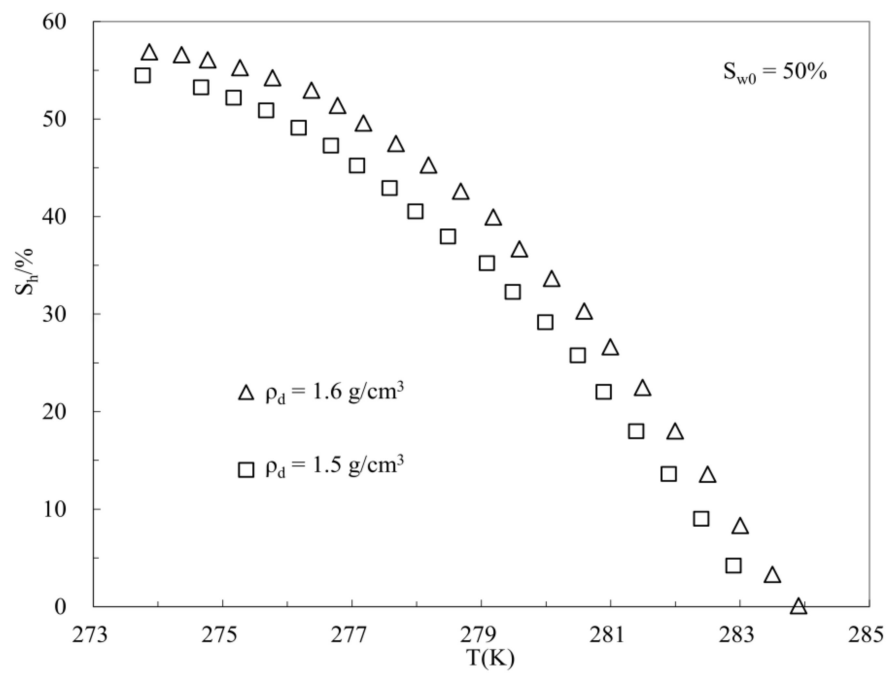
Figure 7. The stability conditions of methane hydrate in fine-grained sediment with different initial water saturation and bulk data [35].

Figure 7 shows the stability conditions of methane hydrate under different initial water saturation. Under the same dry density, as initial water saturation increases, the stability condition curve of methane hydrate in fine-grained sediment exhibits a more significantly left shift from that of bulk hydrate. This is mainly due to the fact that, in the case of low initial water saturation, water is mainly adsorbed on the surface of fine soil particles and the activity of water is low, which leads to higher pressure and lower temperature for stabilizing the methane hydrate.

Figure 8 presents the evolution of hydrate saturation against temperature. From Figure 8, it can be seen that the hydrate saturation decreases with increasing temperature. The increasing temperature causes the methane hydrate dissociation, reducing the content of hydrate within fine-grained sediment. In Figure 8a,b, one can find that the decreasing tendencies in hydrate saturation with temperature for different dry densities are almost consistent with each other, if the influence of initial hydrate saturation is ignored. In Figure 8c, the hydrate saturation evolution curve with temperature is presented at the same dry density. The curves of S_h-T are completely different for the different initial water saturations. For the high initial water saturation, the decrease in hydrate saturation with increasing temperature is relatively uniform. With respect to the low initial water content, the reduction of hydrate saturation is flat at a low temperature stage ($< \sim 280$ K), but sharply decreases when temperature increases up to the temperature of ~ 280 K. This is due to the fact that, under the same initial temperature and pressure, the pore water in the soil sample prefers to exist within small pores and close to the surface of fine soil particles due to the physical adsorption and capillary effect. In the case of the low initial water saturation, pore water is mainly affected by the adsorption effect, and the temperature change does not induce a significant hydrate dissociation. In contrast, high initial water content mainly corresponds to the capillary effect. A great deal of hydrate can be decomposed by increasing temperature at low temperature stage.



(a)



(b)

Figure 8. Cont.

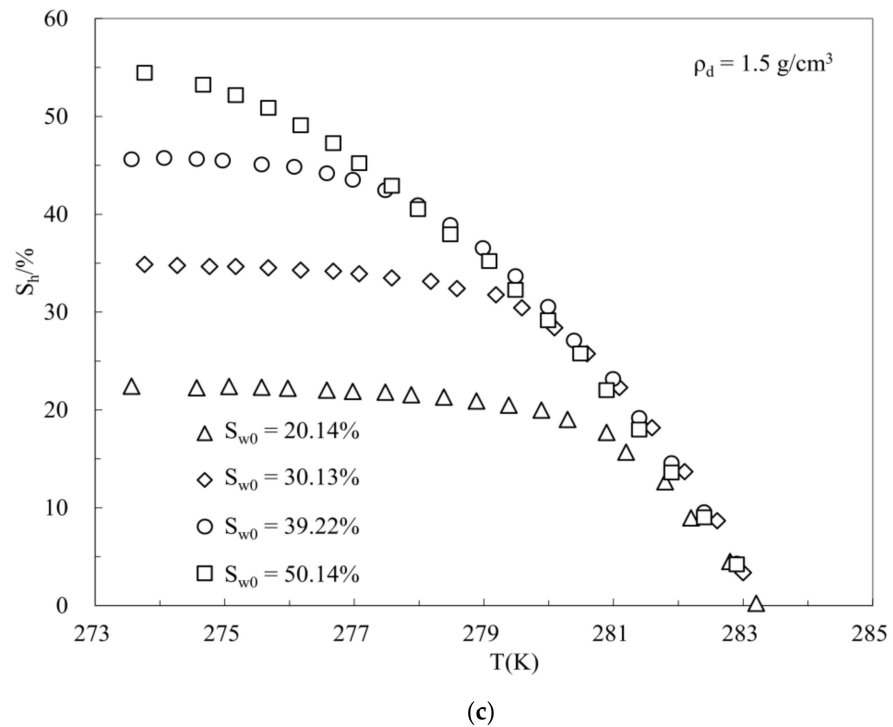


Figure 8. Temperature dissociation curve of methane hydrate in fine-grained sediment. (a) Low initial water saturation; (b) high initial water saturation; (c) different saturation at the same dry density.

3.2. NMR Measurement Results

Figure 9 shows the P–T evolution curve of the synthesis and decomposition of methane hydrate in fine-grained sediment determined by the gas hydrate NMR measurement system, which is consistent with the results measured by the gas hydrate phase equilibrium test system. Figure 9 also finds that the evolution curve of P–T is relatively flat in the early stage of heating. After the experimental temperature reached 7 °C, the slope of the P–T evolution curve increased obviously, indicating that the main dissociation of hydrate also began to increase. The specific reason can be explained by the T_2 (T_2 is the transverse relaxation time; it is proportional to pore radius.) distribution obtained by NMR experiments, as shown in Figure 10.

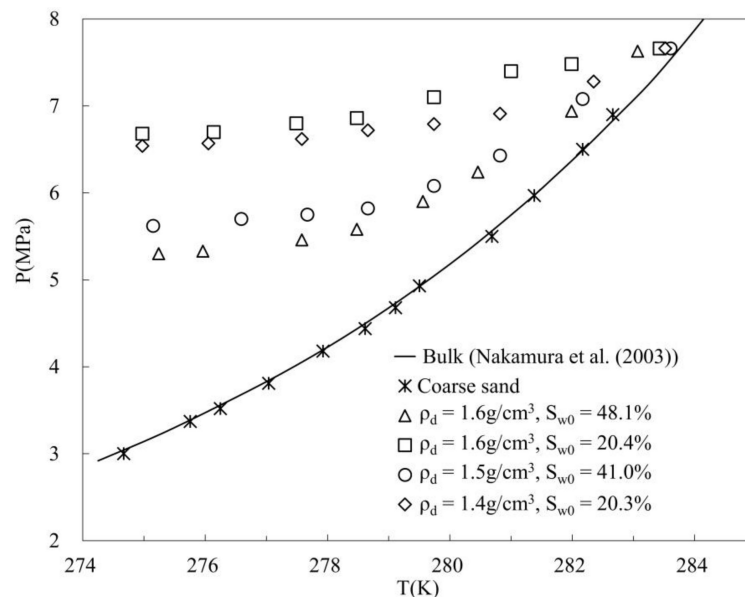


Figure 9. P–T evolution curve of methane hydrate in fine-grained sediment and bulk data [35].

Figure 10 shows the results of signal changes during hydrate synthesis and decomposition in sediments with different dry densities and initial water saturation measured by nuclear magnetic resonance instruments. In the procedure of the test, the temperature is always larger than 1.6 °C not only for ensuring the good synthesis of hydrate, but also for avoiding the effect of freezing on hydrate formation. It can be seen from Section 2.1.2 that the T_2 is proportional to the pore radius R , so the water content in the sample can be determined through the T_2 distribution condition. When there is no methane, only the leftmost T_2 peak appeared, but after the methane gas injection, the second T_2 peak and the rightmost T_2 peak (the third T_2 peak) appeared, and the region of the first T_2 peak enlarged. During the formation and decomposition of methane hydrates, the first and second T_2 peaks change visibly, while the third T_2 peak shows no significant change. The results show that the first and second zeniths are the signals of water and methane in the pores, while the third zenith is the signal intensity of methane gas outside the samples in the measured area.

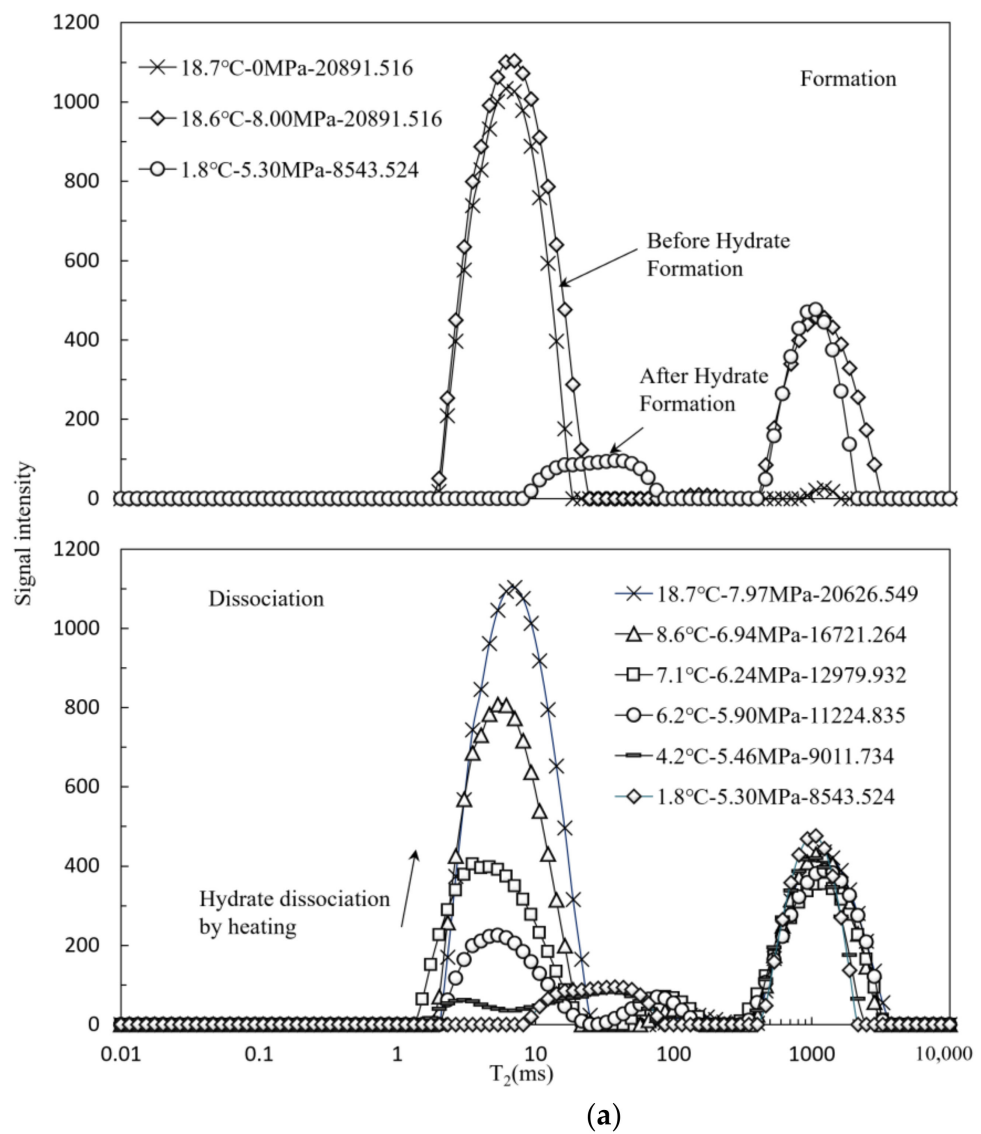


Figure 10. Cont.

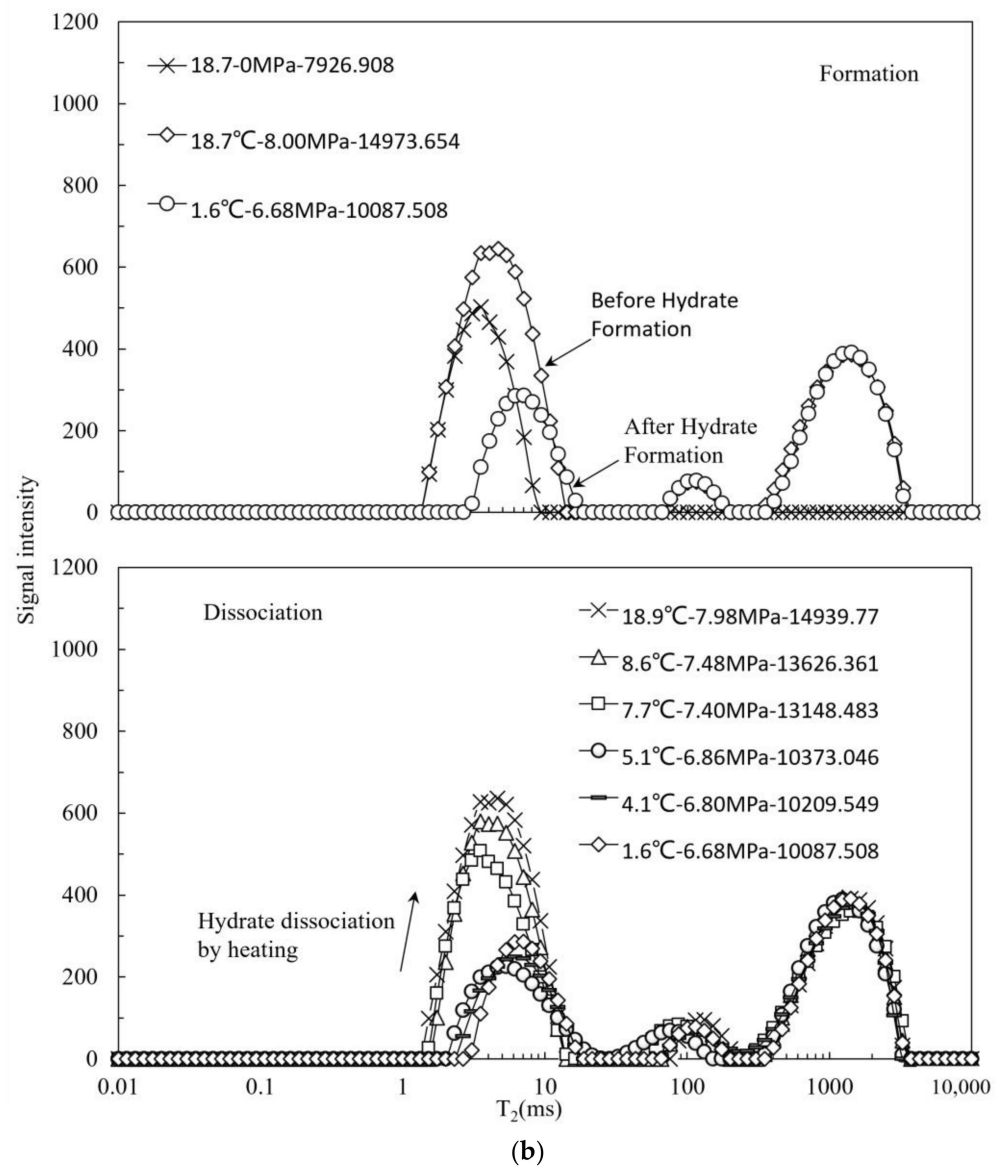


Figure 10. Cont.

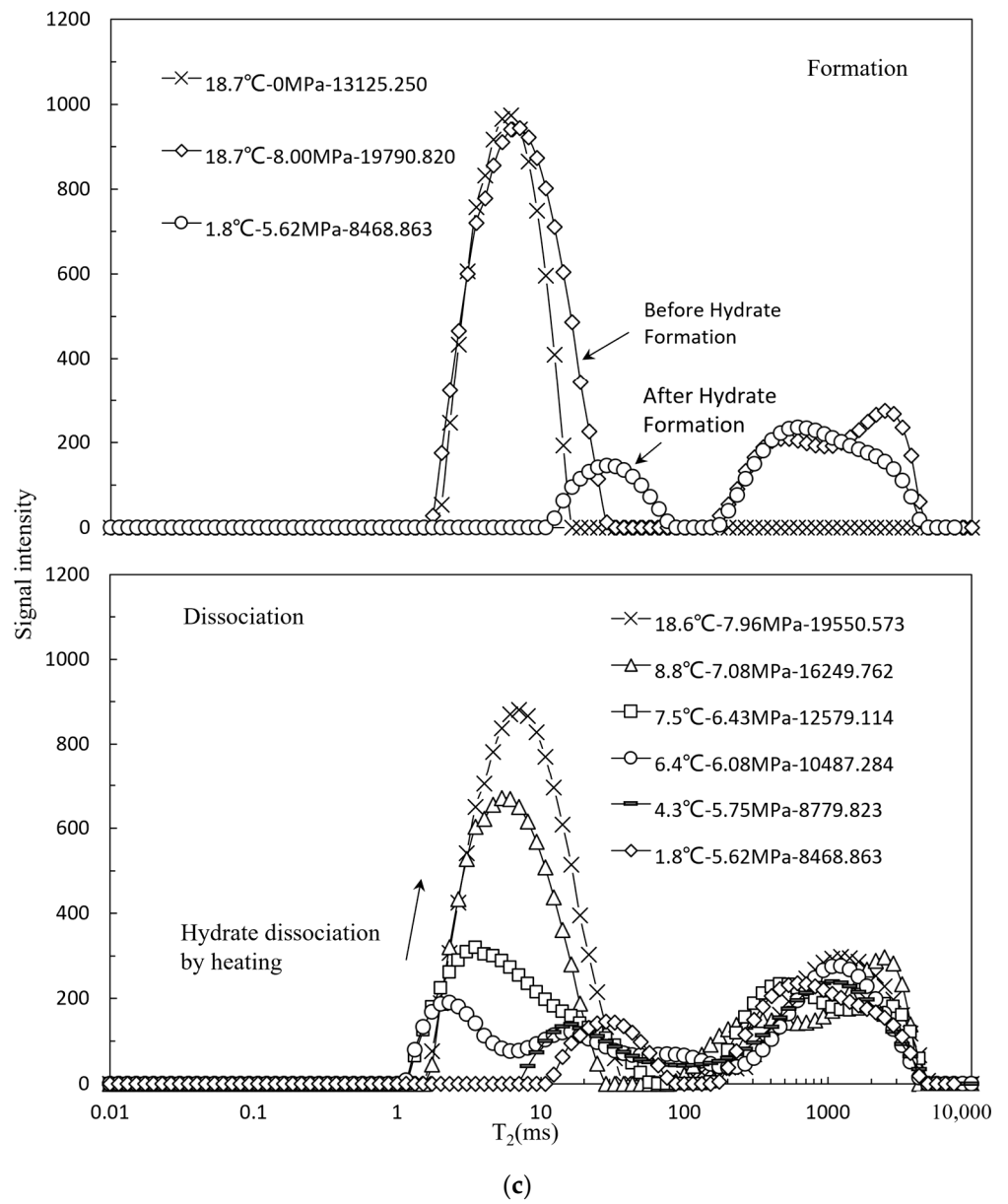


Figure 10. Cont.

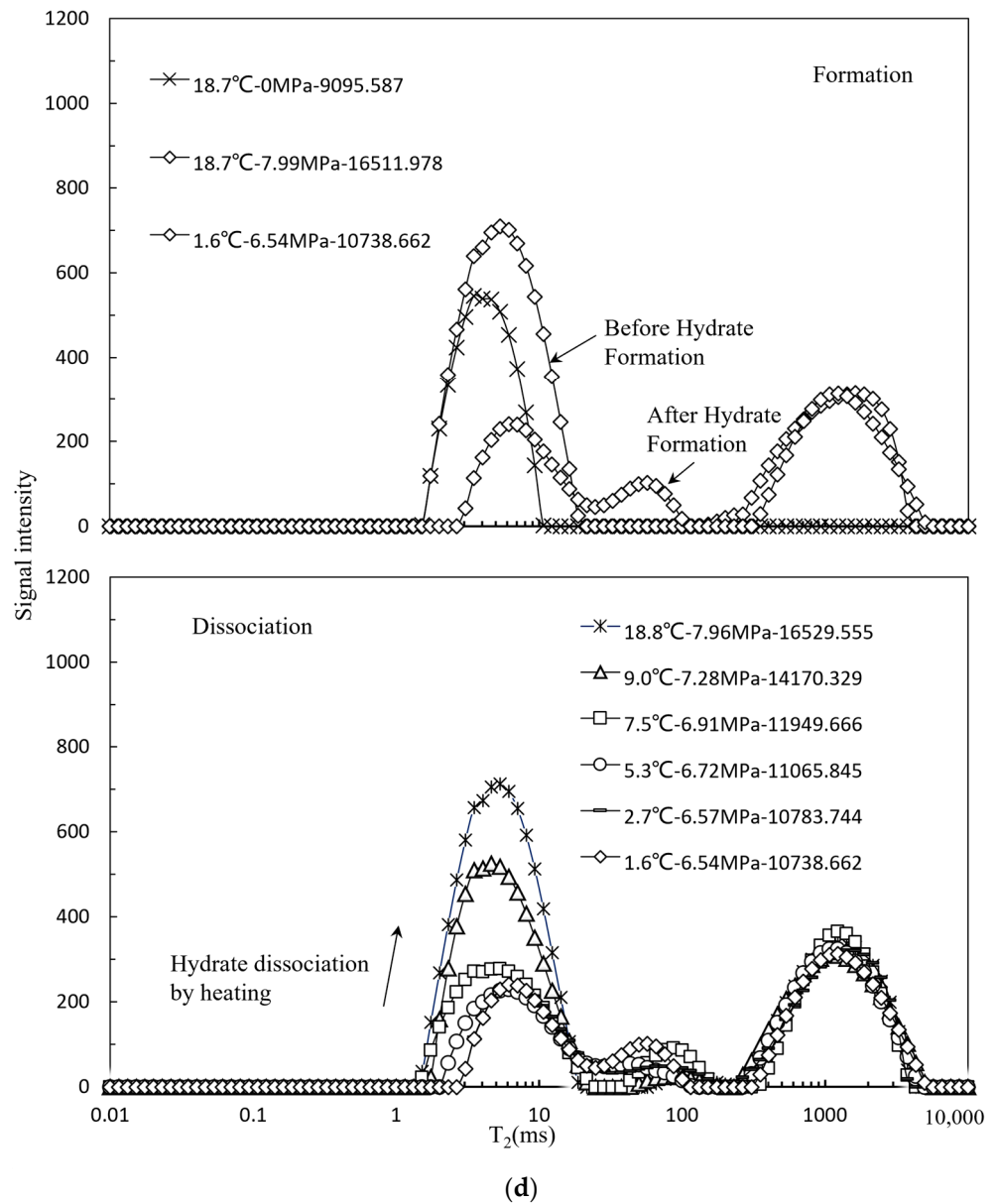


Figure 10. T_2 distribution curve during synthesis and decomposition of methane hydrate in silt. (a) $\rho_d = 1.6 \text{ g/cm}^3$, $S_{W0} = 48.10\%$; (b) $\rho_d = 1.6 \text{ g/cm}^3$, $S_{W0} = 20.40\%$; (c) $\rho_d = 1.5 \text{ g/cm}^3$, $S_{W0} = 41.00\%$; (d) $\rho_d = 1.4 \text{ g/cm}^3$, $S_{W0} = 20.30\%$.

As shown in Figure 10, the nuclear magnetic signal intensity increases inhomogeneously with decomposition time. The small pores corresponding to T_2 at 1~2 ms have no nuclear magnetic signal intensity at the hydrate synthesis stage, but the signal intensity suddenly appears after heating and dissociation in the early stage (temperature up to 7 °C). In the later period of heating, the NMR signal intensity of the aperture range has no obvious change, but the change in the signal intensity is more significant in the large aperture. This shows that the hydrate in the small pores basically decomposes completely in the early stage, and the decomposition rate of methane hydrate in the macropores increases when the temperature reaches 7 °C. The reason for this phenomenon is probably that the water in the small pores is more significantly affected by the physical adsorption on the surface of mineral particles and the capillary effect of the pores, so that the potential energy of the small pores is lower and the required equilibrium conditions are harsh. It is also sensitive to the change of temperature and pressure environment. Macropores are greatly affected by armor effect [39], which leads to the existence of some residual water. When the tempera-

ture reaches 7 °C, the temperature and pressure condition is close to the phase equilibrium line, so the decomposition rate of methane hydrate in macropores is accelerated. This is also the reason why the slope of the P–T evolution curve in Figure 9 increases obviously. In addition, it can be seen from Figure 10 that the positions of the first two T₂ peaks of the samples with high initial water saturation (such as Figure 10a,c) have changed obviously, while those of the samples with low initial water saturation (such as Figure 10b,d) have not shifted obviously. This is probably due to the formation of methane hydrate on the surface of soil particles caused by the secondary synthesis of liquid water hydrate produced by decomposition, which promotes the change in surface relaxation rate, especially the migration of water in the samples with high water saturation.

3.3. Stability Conditions Simulation

At present, most of the hydrate stability condition models are based on the van der Waals-Platteeuw (later known as vdWP) model [40–43]. Clarke et al. [40] only considered the influence of a single pore diameter and could not establish a unified relationship between pore size variation and stability conditions. Klauda and Sandler [41] further extended the vdWP model by using the probability model of pore size. Yan et al. [42] established a stability condition model of hydrate in porous media by linking the water holding characteristic curve with the synthetic conditions of hydrate. Zhou et al. [43] proposed a generalized phase equilibrium equation by combining the equilibrium condition of hydrate in sediment with the capillary effect and salt concentration. For this reason, this section will deepen and expand the Brooks and Corey [44] model theory and present a methane hydrate stability condition model suitable for the fine-grained sediment with wild pore size distribution characteristic.

According to the Gibbs–Thomson equation, the temperature offset $\Delta T (\Delta T = T_{bulk} - T_s)$ of the equilibrium temperature of hydrate in capillary from pure hydrate can be calculated by [45]:

$$\Delta T = T_{bulk} / (\rho_h \Delta H) p_c \tag{4}$$

$$p_c = F \gamma_{hl} \cos \theta / r \tag{5}$$

where p_c represents the capillary suction at the hydrate–water interface at the hydrate phase transition region within sediment pores, ΔH is the enthalpy of formation of methane hydrate ($\Delta H = 338.7$ kJ/kg) [45], γ_{hl} represents the interfacial tension between hydrate and water, θ indicates the contact angle between hydrate and pore wall of sediment, and r is the pore radius. T_{bulk} is the equilibrium temperature of pure hydrate, which can be obtained by being fitted from the stability condition curve of methane hydrate measured by Nakamaura et al. [35] in this paper. In this study, $T_{bulk} = 9.737 \ln p + 263.9$.

T_s is the stable temperature of hydrate in sediment, which can be obtained by:

$$T_s = T_{bulk} - \Delta T = T_{bulk} - T_{bulk} / (\rho_h \Delta H) p_c \tag{6}$$

According to the Formulas (4)–(6), the temperature and pressure conditions after the equilibrium of water in a single radius sediment can be obtained. However, due to the synthesis of hydrate, the pore size changes all the time, so the capillary pressure in the formula also changes. According to the research conclusion of Yan et al. [42] and Zhou et al. [43], the relationship between capillary pressure and water saturation is similar to the soil–water characteristic curve of the sample. Therefore, the soil–water characteristic curve model of Brooks & Corey [44] is used to describe the relationship between capillary pressure and water saturation as:

$$p_c = a((S_w - S_w^r) / (1 - S_w^r))^{-n} \tag{7}$$

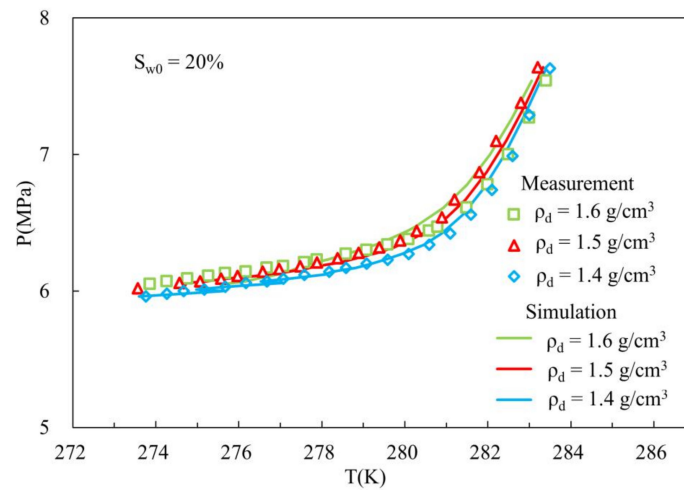
where S_w represents undehydrated water saturation in each period, S_w^r represents residual water saturation after hydrate formation in sediments in theory, and a and n are model parameters.

Through combining the above three Equations (5)–(7), the stability conditions of hydrate in fine-grained sediments can be obtained, which is the relationship of temperature T , pressure P , and unhydrated water saturation S_w . However, it is worth noting that the capillary pressure in Equation (7) does not address the influence of dense degree on stability condition. Thus, the authors improve the model parameters according to the relationship established by Yan et al. [46] as:

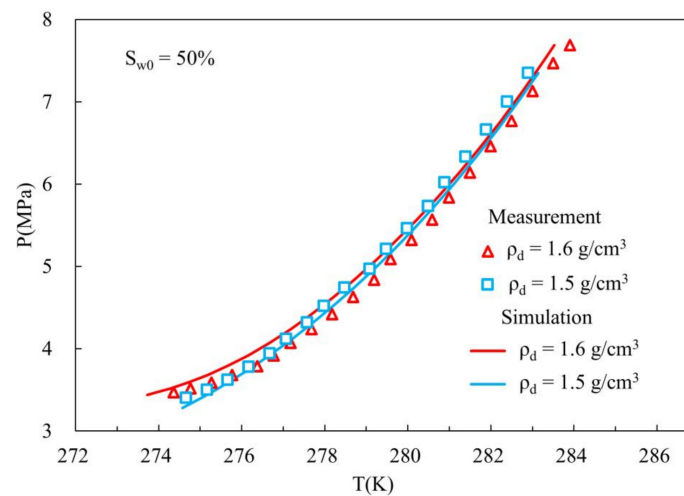
$$a = \eta e^\omega \tag{8}$$

where e is void ratio of sediment, and parameters η and ω are fitting parameters.

To verify the model, a series of experimental samples (marked by A1, A2, B1, B2, B3, B4, and C1) are simulated. The used parameters are listed as followings: $\eta = 70$, $\omega = -2$, $n = 0.8$. Due to the discrepancy in sample preparation with different dry density and initial water saturation, the residual water content is completely different. Therefore, this simulation adopts different values for A1, A2, B1, B2, B3, B4, and C1. The adopted values for S_w^r are 0.1%, 0.01%, 1.82%, 1.8%, 1.65, 1%, and 1.5% for A1, A2, B1, B2, B3, B4, and C1, respectively. The simulation results are shown in Figure 11, and the predicted result of the model satisfactorily coincides with the experimental data. It has been demonstrated that the established model is capable of addressing the stability condition of methane hydrate within fine-grained sediment.



(a)



(b)

Figure 11. Cont.

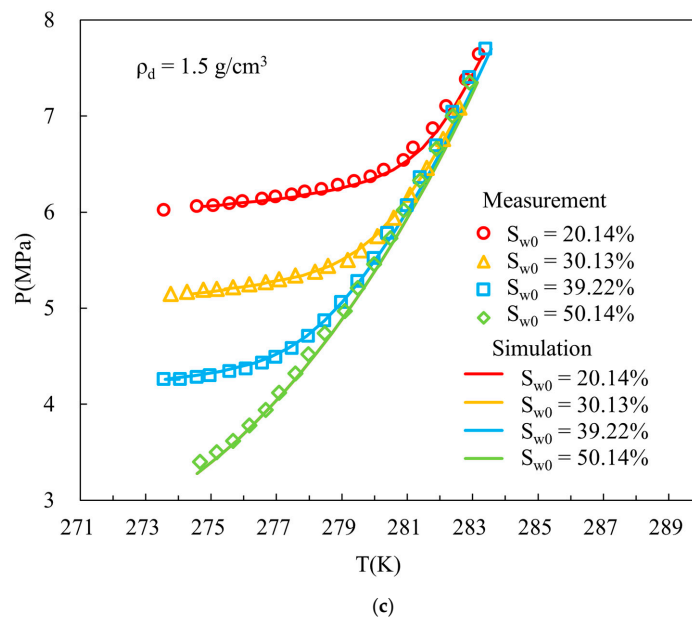


Figure 11. Comparison of simulation results of measured equilibrium conditions of methane hydrate phase in fine-grained sediment. (a) Low initial water saturation; (b) high initial water saturation; (c) different saturation at the same dry density.

4. Conclusions

This paper measures the stability condition of methane hydrate within artificially prepared fine-grained sediment through the multi-step temperature rising method. The NMR technique is used to reveal the formation and dissociation procedure of methane hydrate within fine-grained sediment. In addition, an improved model is established to address the stability condition of methane hydrate in fine-grained sediment:

The stable temperature and pressure condition of methane hydrate within fine-grained sediment deviates left from that of the bulk methane hydrate. The dry density has a slighter influence on the stability condition, but the capillary suction can play a significant role in influencing the stability condition of methane hydrate at low initial water content.

The NMR result suggests that methane hydrate in fine-grained sediment is not completely synthesized because of the physical adsorption and capillary effect. In the hydrate dissociation, the hydrate in the small pores decomposes first, then followed by the larger sediment pores.

The developed model for stability condition of methane hydrate links the relationship of pressure, temperature, and undydrated water saturation within fine-grained sediment. As validated by the measured data, the model is demonstrated to have the ability of simulating the stability condition of methane hydrate in fine-grained sediment, especially for the influences of initial water content and dry density.

Author Contributions: Conceptualization, D.L. and Q.T.; formal analysis, R.Y. and S.T.; visualization, Y.C.; writing—original draft, D.L.; writing—review and editing, R.Y. and D.Y.; funding acquisition R.Y. and D.Y. All authors have read and agreed to the published version of the manuscript.

Funding: This research was funded by the Natural Science Foundation of China under Grants (No. 11962004) and (No. 12262009), and the Open Fund of Guangxi Key Laboratory of Geomechanics & Geotechnical Engineering (No. 22-Y-KF-01).

Institutional Review Board Statement: Not applicable.

Informed Consent Statement: Not applicable.

Data Availability Statement: The data that support the findings of this study are available within the article.

Conflicts of Interest: The authors declare no conflict of interest.

References

1. Kvenvolden, K.A. Gas hydrates—Geological perspective and global change. *Rev. Geophys.* **1993**, *31*, 173–187. [[CrossRef](#)]
2. Makogon, Y.F.; Holditch, S.A.; Makogon, T.Y. Natural gas-hydrates—A potential energy source for the 21st Century. *J. Pet. Sci. Eng.* **2007**, *56*, 14–31. [[CrossRef](#)]
3. Liu, L.L.; Zhang, X.H.; Lu, X.B. Review on the permeability of hydrate-bearing sediments. *Adv. Earth Sci.* **2012**, *27*, 733–746.
4. Kong, L.; Liu, W.Z.; Yuan, Q.M.; Dong, T. Triaxial tests on gassy sandy soil under constant shear stress paths. *Rock Soil Mech.* **2019**, *40*, 3319–3326.
5. Pan, Z.; Liu, Z.M.; Liu, D.J.; Shang, L.Y.; Li, W.Z.; Li, P. Research progress on influence factors of natural gas hydrate formation in porous media. *Chem. Ind. Eng. Prog.* **2017**, *12*, 4403–4414.
6. Marshall, D.R.; Saito, S.; Kobayashi, R. Hydrates at high pressures: Part I. Methane-water, argon-water, and nitrogen-water systems. *AIChE J.* **1964**, *10*, 202–205. [[CrossRef](#)]
7. Kobayashi, R.; Katz, D.L. Methane Hydrate at high pressure. *J. Petrol. Technol.* **1949**, *186*, 66–70. [[CrossRef](#)]
8. Clennell, M.B.; Hovland, M.; Booth, J.S.; Henry, P.; Winters, W.J. Formation of natural gas hydrates in marine sediments 1. Conceptual model of gas hydrate growth conditioned by host sediment properties. *J. Geophys. Res. Solid Earth* **1999**, *104*, 22985–23003. [[CrossRef](#)]
9. Handa, Y.P.; Stupin, D.Y. Thermodynamic properties and dissociation characteristics of methane and propane hydrates in 70-Å-radius silica gel pores. *J. Phys. Chem.* **1992**, *96*, 8599–8603. [[CrossRef](#)]
10. Uchida, T.; Ebinuma, T.; Ishizaki, T. Dissociation condition measurements of methane hydrate in confined small pores of porous glass. *J. Phys. Chem. B* **1999**, *103*, 3659–3662. [[CrossRef](#)]
11. Uchida, T.; Ebinuma, T.; Takeya, S.; Nagao, J.; Narita, H. Effects of pore sizes on dissociation temperatures and pressures of methane, carbon dioxide, and propane hydrates in porous media. *J. Phys. Chem. B* **2002**, *106*, 820–826. [[CrossRef](#)]
12. Anderson, R.; Llamedo, M.; Tohidi, B.; Narita, R.W. Experimental measurement of methane and carbon dioxide clathrate hydrate equilibria in mesoporous silica. *J. Phys. Chem. B* **2003**, *107*, 3507–3514. [[CrossRef](#)]
13. Linga, P.; Haligva, C.; Nam, S.C.; Englezos, P. Recovery of methane from hydrate formed in a variable volume bed of silica sand particles. *Energy Fuels* **2009**, *23*, 5508–5516. [[CrossRef](#)]
14. Bagherzadeh, S.A.; Moudrakovski, I.L.; Ripmeester, J.A.; Englezos, P. Magnetic resonance imaging of gas hydrate formation in a bed of silica sand particles. *Energy Fuels* **2011**, *25*, 3083–3092. [[CrossRef](#)]
15. Turner, D.J.; Cherry, R.S.; Sloan, E.D. Sensitivity of methane hydrate phase equilibria to sediment pore size. *Fluid Phase Equilibria* **2005**, *228*, 505–510. [[CrossRef](#)]
16. Boswell, R. Is gas hydrate energy within reach? *Science* **2009**, *325*, 957–958. [[CrossRef](#)]
17. Wang, X.J.; Hutchinson, D.R.; Wu, S.G.; Yang, S.X.; Guo, Y.Q. Elevated gas hydrate saturation within silt and silty clay sediments in the Shenhu area, South China Sea. *J. Geophys. Res. Solid Earth* **2011**, *116*, B051022011. [[CrossRef](#)]
18. Zhang, G.X.; Liang, J.Q.; Lu, J.A.; Yang, S.X.; Zhang, M.; Holland, M.N.; Peter, S.T.; Su, X.; Sha, Z.B.; Xu, H.N.; et al. Geological features, controlling factors and potential prospects of the gas hydrate occurrence in the east part of the Pearl River Mouth Basin, South China Sea. *Mar. Pet. Geol.* **2015**, *67*, 356–367. [[CrossRef](#)]
19. Yan, R.T.; Wei, H.Z.; Wu, E.L.; Wang, S.Y.; Wei, C.F. A phase equilibrium model for gas hydrates considering pore-size distribution of sediments. *Acta Phys. Chim. Sin* **2011**, *27*, 295–301.
20. Kumar, A.; Sakpal, T.; Roy, S.; Kumar, R. Methane hydrate formation in a test sediment of sand and clay at various levels of water saturation. *Can. J. Chem.* **2015**, *93*, 874–881. [[CrossRef](#)]
21. Matsushima, J.; Ali, M.Y.; Roy, S.; Bouchaala, F. Attenuation estimation from sonic logging waveforms combining seismic interferometry and common mid-point approach. *Geophysics* **2017**, *83*, 21–35. [[CrossRef](#)]
22. Bouchaala, F.; Guennou, C. Estimation of viscoelastic attenuation of real seismic data by use of raytracing software: Application to the detection of gas hydrates and free gas. *Energy Procedia* **2012**, *344*, 57–66.
23. Sun, S.C.; Liu, C.L.; Ye, Y.G.; Liu, Y.F. Pore capillary pressure and saturation of methane hydrate bearing sediments. *Acta Oceanol. Sin.* **2014**, *33*, 30–36. [[CrossRef](#)]
24. Liu, C.L.; Ye, Y.G.; Sun, S.C.; Chen, Q.; Meng, Q.G.; Hu, G.W. Experimental studies on the P-T stability conditions and influencing factors of gas hydrate in different systems. *Sci. China Earth Sci.* **2013**, *56*, 594–600. [[CrossRef](#)]
25. Liu, C.L.; Meng, Q.G.; Hu, G.W.; Li, C.F.; Sun, J.Y.; He, X.L.; Wu, N.Y.; Yang, S.X.; Liang, J.Q. Characterization of hydrate-bearing sediments recovered from the Shenhu area of the South China Sea. *Interpretation* **2017**, *5*, SM13–SM23. [[CrossRef](#)]
26. Ji, Y.K.; Hou, J.; Cui, G.D.; Liu, Y.L.; Du, Q.G. Experimental study on methane hydrate formation in a partially saturated sandstone using low-field NMR technique. *Fuel* **2019**, *25*, 82–90. [[CrossRef](#)]
27. Ji, Y.K.; Hou, J.; Zhao, E.M.; Lu, N.; Bai, Y.J.; Zhou, K.; Liu, Y.G. Study on the effects of heterogeneous distribution of methane hydrate on permeability of porous media using low-field NMR technique. *J. Geophys. Res. Solid Earth* **2020**, *125*, e2019JB018572. [[CrossRef](#)]
28. Davidson, D.W.; Garg, S.K.; Gough, S.R.; Handa, Y.P.; Ratcliffe, C.I.; Ripmeester, J.A.; Tse, J.S.; Lawson, W.F. Laboratory analysis of a naturally occurring gas hydrate from sediment of the Gulf of Mexico. *Geochim. Cosmochim. Acta* **1968**, *50*, 619–623. [[CrossRef](#)]

29. Hupp, D.; Burt, J.; Blades, A.J. Petrophysical evaluation of natural gas hydrates-north slope, Alaska. In Proceedings of the SPE Western Regional Meeting, Anchorage, AK, USA, 23–26 May 2016.
30. Ratcliffe, C.I.; Ripmeester, J.A. ^1H and ^{13}C NMR studies on carbon dioxide hydrate. *J. Phys. Chem.* **1986**, *90*, 1259–1263. [[CrossRef](#)]
31. Uchida, T.; Hirano, T.; Ebinuma, T.; Ishizaki, T.S. Raman spectroscopic determination of hydration number of methane hydrates. *AIChE J.* **1999**, *45*, 2641–2645. [[CrossRef](#)]
32. Madhusudhan, B.N.; Clayton, C.R.I.; Priest, J.A. The effects of hydrate on the strength and stiffness of some sands. *J. Geophys. Res. Solid Earth* **2019**, *124*, 65–75. [[CrossRef](#)]
33. Malagar, B.R.C.; Lijith, K.P.; Singh, D.N. Formation & dissociation of methane gas hydrates in sediments: A critical review. *J. Nat. Gas Sci. Eng.* **2019**, *65*, 168–184.
34. Peng, D.Y.; Robinson, D.B. A new two parameters Equation of State. *Ind. Eng. Chem. Fundam.* **1976**, *15*, 59–64. [[CrossRef](#)]
35. Nakamura, T.; Makino, T.; Sugahara, T.; Ohgaki, K. Stability boundaries of gas hydrates helped by methane—Structure-H hydrates of methylcyclohexane and cis-1, 2-dimethylcyclohexane. *Chem. Eng. Sci.* **2003**, *58*, 269–273. [[CrossRef](#)]
36. Chen, Q.; Ye, Y.G.; Liu, C.L.; Diao, S.B.; Zhang, J. Simulation experiment on the kinetics of methane hydrate formation in porous media. *Mar. Geol. Quat. Geol.* **2007**, *27*, 111–116.
37. Turner, D.; Sloan, D. Hydrate phase equilibrium measurements and predictions in sediments. In Proceedings of the Fourth International Conference on Gas Hydrates, Yokohama, Japan, 19–23 May 2002.
38. Shun, S.C.; Ye, Y.G.; Liu, C.L.; Tan, Y.Z.; Meng, Q.G.; Ma, Y.; Xiang, F.K. Preliminary Experiment of Stable p-T Conditions of Methane Hydrate in. *Geoscience* **2010**, *24*, 638–642.
39. Shun, S.C.; Ye, Y.G.; Liu, C.L.; Wei, W.; Zhao, N.; Xiang, F.K.; Ma, Y. Research of methane hydrate formation process in quartzsand. *Chem. Eng. Oil Gas* **2011**, *40*, 123–127.
40. Clarke, M.A.; Pooladi-Darvish, M.; Bishnoi, P.R. A method to predict equilibrium conditions of gas hydrate formation in porous media. *Ind. Eng. Chem. Res.* **1999**, *38*, 2485–2490. [[CrossRef](#)]
41. Klauda, J.B.; Sandler, S.I. Predictions of gas hydrate phase equilibria and amounts in natural sediment porous media. *Mar. Pet. Geol.* **2003**, *20*, 459–470. [[CrossRef](#)]
42. Yan, R.T.; Mu, C.M.; Zhang, Q.; Tian, H.H.; Zhou, J.Z.; Wei, C.F. A phase equilibrium model for hydrate in sediment accounting for pore capillary effect (in Chinese). *Sci. Sin.-Phys. Mech. Astron.* **2019**, *49*, 034607. [[CrossRef](#)]
43. Zhou, J.Z.; Liang, W.P.; Wei, C.F. Phase Equilibrium Condition for Pore Hydrate: Theoretical Formulation and Experimental Validation. *J. Geophys. Res. Solid Earth* **2019**, *124*, 703–721. [[CrossRef](#)]
44. Brooks, R.; Corey, A. *Hydraulic Properties of Porous Media*; Hydrology Paper, No. 3; Civil Engineering Department, Colorado State University: Fort Collins, CO, USA, 1964.
45. Sun, S.C.; Liu, C.L.; Ye, Y.G.; Liu, Y.F. Phase behavior of methane hydrate in silica sand. *J. Chem. Thermodyn.* **2014**, *69*, 118–124. [[CrossRef](#)]
46. Yan, R.T.; Hayley, J.L.; Priest, J.A. Modeling the water retention curve of hydrate-bearing sediment. *Int. J. Geomech.* **2020**, *20*, 04019179. [[CrossRef](#)]

Disclaimer/Publisher’s Note: The statements, opinions and data contained in all publications are solely those of the individual author(s) and contributor(s) and not of MDPI and/or the editor(s). MDPI and/or the editor(s) disclaim responsibility for any injury to people or property resulting from any ideas, methods, instructions or products referred to in the content.